



Optimization of process parameters for 4643 Al alloy anodization in mixed oxalic/phosphoric electrolytes: Doehlert experimental design

Khalid H. Rashid^{a,1}, Anees A. Khadom^{b,*,2} , Abdul Amir H. Kadhum^{c,3}

^a Department of Chemical Engineering, University of Technology-Iraq, Baghdad, Iraq

^b Department of Chemical Engineering, College of Engineering, University of Diyala, Baquba City, Daiyla governorate 32001, Iraq

^c University of Al-Ameed, Karbala, Iraq

ARTICLE INFO

Keywords:

Aluminum
Optimization
Corrosion
Anodizing
Oxalic acid
Phosphoric acid

ABSTRACT

The anodization technology is commonly used for surface enhancement for aluminum and its alloys. It is widely used to improve the hardness and corrosion resistance of aluminum alloys. In the present work, the Doehlert experimental design was used to optimize the film generated on aluminum during anodization in oxalic or phosphoric solutions. The research assessed the oxide layer thickness (T_{OL}) and practical oxide layer efficiency (η_{POLE}) based on variables such as temperature, electrolyte concentration, current density, and exposure duration. According to the Doehlert experimental design, 25 tests are achieved for each response function. The anodized aluminum samples are tested in an aggressive saline solution via electrochemical techniques. The open-circuit potential measurements showed that steady-state potentials are approached after 40 minutes. The polarization measurements showed that corrosion current density decreased with an increase in layer thickness. Maximum protection efficiency was 97 % at optimum layer thickness. Electrochemical impedance spectroscopy measurements indicated that the metal's resistance increased with the thickness of the layer, corroborating the polarization findings. The outcomes of the experimental design and mathematical modeling show that all process-independent variables are significant. Furthermore, the interaction between the independent variables on the thickness of the oxide layer and the practical oxide layer efficiency is very considerable. The optimum T_{OL} and η_{POLE} are 25.5459 μm and 0.976, respectively. These results were further validated through surface morphology analyses.

1. Introduction

Aluminum alloys are extensively utilized due to their lightweight nature, high specific strength, and ease of formation [1]. Despite these advantages, their poor corrosion resistance and low hardness restrict their application and longevity. Aluminum naturally develops a protective oxide layer in the presence of oxygen [2], which can be enhanced through anodizing to improve corrosion resistance [3]. This method produces a coating (porous anodic alumina layer) on the surface of aluminum [4]. Several electrolytes have been explored to achieve the anodic oxidation process, with H_2SO_4 electrolyte being the most often employed in industry due to its electrolyte stability, cost-effectiveness, and the characteristics of the resultant film [5]. However, H_2SO_4

electrolyte is corrosive to the porous anodic alumina film with limited film hardness [6]. Commonly, the porous alumina films were studied by many other aqueous solutions to enlarge or modify the surface morphology and enhance the corrosion resistance [7–9]. Nakajima et al. [10] investigated the growth behavior of anodic oxide films during the anodizing process using ketoglutaric, glutaric, and acetonedicarboxylic acid solutions. Glutaric acid was used to produce a thin layer of anodic oxide on the metal surface. In contrast, the use of ketoglutaric and acetonedicarboxylic acids in the anodizing process produced a thick anodic porous alumina sheet due to their low acid dissociation constants. These findings indicate that acid dissociation constants are critical in the production of anodic porous alumina. Sarganov and Gorokh [11] studied the development kinetics of aluminum oxide coatings while

* Corresponding author.

E-mail addresses: khalid.h.rashid@uotechnology.edu.iq (K.H. Rashid), aneesdr@gmail.com (A.A. Khadom), amir1719@gmail.com (A.A.H. Kadhum).

¹ ORCID: 0000-0002-6605-1092

² ORCID: 0000-0003-2284-6325

³ ORCID: 0000-0003-4074-9123

anodizing tartaric acid electrolyte at a constant current density. Researchers discovered that the highest number of oxide cells is $9.2 \times 10^8 \text{ cm}^{-2}$. Mozalev et al. [12] investigated the anodizing behavior of aluminum in citric acid solutions by altering current density, concentration, electrolyte temperature, and agitating. Their results indicated that the characteristics of the barrier layer were directly proportional to the formation voltage. Kikuchi et al. [13] demonstrated the creation of aluminum anodic oxide by anodizing in pyrophosphoric acid, achieving a nanofiber density of 10^{10} nanofibers/cm² during the process. In a separate study, Kikuchi et al. [14] fabricated a highly ordered anodic porous alumina using etidronic acid anodizing, forming nanostructures with cell diameters ranging from 530 to 670 nm under constant current density.

The anodizing process can be conducted using a combination of acids. Saeedikhani et al. [15] used a mixed electrolyte containing 10 % sulfuric acid, 5 % boric acid, and 2 % phosphoric acid to anodize 2024 aluminum alloy. This was followed by a sealing process. Their findings indicated that the mixed acid electrolyte enhanced the corrosion resistance and durability. Shang et al. [16] investigated the anodizing process of Al alloy in sulfuric/oxalic acid, sulfuric/citric acid, and sulfuric acid/tartaric acid mixed electrolytes. The mixed electrolytes have improved the corrosion resistance of the metal. The average corrosion rate was 7.3, 6, and 7.5 mg/h.m² for sulfuric/oxalic acid, sulfuric/citric acid, and sulfuric acid/tartaric acid, respectively, as compared with 9.7 mg/h.m² for sulfuric acid alone. Lu et al. [17] found that the corrosion resistance was enhanced for the anodizing process of the 2024 Al alloy using mixed acid electrolytes (malonic acid+ H₂SO₄). Capelossi et al. [18] anodized aluminum alloy using a tartaric acid and sulfuric acid mixture. The addition of tartaric acid improved the corrosion resistance.

Anodizing process parameters play an important role in demining film properties. Therefore, optimization techniques can be applied. It is essential to apply a proper design in the optimization process. A linear or quadratic model can be used for data correlation by experimental design, such as Box-Behnken Design, Central Composite Design, and Doehlert Design [19]. These designs are classified as response surface designs or surface response methodology (RSM). The number of experiments is reduced by using Doehlert designs [20]. The response function is correlated to all variables at different levels. Then critical points (maximum, minimum, or saddle) can be evaluated. Doehlert design is more efficient than some other central composite designs [21]. In general, the Doehlert design is highly inexpensive, versatile, and efficient in modeling experimental data, in addition to allowing very fascinating flexibility in the selection of levels of the variables under examination as compared with other designs [21]. Bensalah et al. [22] examined the factors affecting the tartaric/sulfuric acid anodizing process using a Doehlert design. They optimized the effects of temperature, anodic current density, and electrolyte concentrations on the properties of the anodic oxide layer. The study focused on four objectives: growth rate, hardness, dissolution rate, and weight loss. The goals were to minimize weight loss and dissolution rate while maximizing hardness and film growth rate. Bargui et al. [23] investigated the optimization of the anodization process for Al 5754 aluminum alloy using sulfuric acid. Using the Doehlert experimental design, they measured the micro-hardness, wear rate, and growth rate of the anodic oxide layer in response to bath temperature, current density, and sulfuric acid concentration. The optimization intended to maximize the development rate and micro-hardness while minimizing the rate of wear, guided by the desirability function. Similarly, Bensalah et al. [24] used a Doehlert experimental design to optimize the mechanical and chemical properties of sulfuric acid-anodized aluminum.

The novelty of this research lies in three main points: the study of the anodic process of 4643 aluminum alloy is limited in the scientific literature. The application of Doehlert experimental design is rarely applied as compared with other experimental designs for the anodization processes. Finally, the use of mixed oxalic/phosphoric acid as an

electrolyte. In our previous works, the aluminum alloys were anodized by using different electrolytes [25,26]. The 5854 aluminum-magnesium alloy was anodized in a sulfosalicylic/oxalic acid electrolyte. The impact of sealing time and electrochemical behavior was assessed [25]. The Box-Wilson central composite design was utilized to optimize the anodizing process of aluminum ASA 6061 with chromic acid. In the current study, the Doehlert experimental design was employed to optimize the anodizing process of 4643 Al alloy using a mixture of oxalic and phosphoric electrolytes. The objective function (film thickness and corrosion current density) was evaluated at four different variables (bath temperature, electrolyte concentration, current density, and exposure time).

2. Experimental and method

2.1. Materials and chemicals

The 4643 aluminum alloy compositions were (wt%): 0.8 Fe, 0.10 Cu, 4.6 Si, 0.05 Mn, 0.15 Ti, 0.10 Zn, 0.30 Mg, and, 93.9 Al. The anodizing procedure was performed at mixed oxalic/phosphoric acid (OPA) electrolytes (25 g/L oxalic acid (0.198 M) dehydrate (C₂H₂O₄·2 H₂O) solution + 150 g/L phosphoric acid (1.531 M)). Distilled water was used during the dilution and cleaning processes.

2.2. Anodizing process and surface characterizations

The anodizing cell was outfitted to provide up to 5 A of current and 60 V of voltage to the electrodes. A sealing process involved immersing the working electrode in boiling distilled water for 10 minutes. The full details of the experimental anodizing process and system installation were given in our previous works [27,28]. A high-accuracy electronic balance was used to measure the weight before tests (W_1), the weight after the anodizing process (W_2), and the weight after removing the anodic coating film (W_3). W_3 was obtained by a stripping in a solution containing 35 ml phosphoric acid (85 %) and chromic acid (20 g per liter) at 94 °C for 15 minutes, then the specimen was rinsed in distilled water to remove the excess solution on the specimen. An optical microscope (Type MeF2, Germany) was used to analyze the microstructure of the anodic coating film. The response functions for anodizing process were the oxide layer thickness (T_{OL}) and the practical oxide layer efficiency (η_{POLE}). These responses were obtained using Eqs. 1 and 2, and they evaluated as a function of temperature, electrolyte concentration, current density, and time.

$$T_{OL} = \frac{W_c}{Sd_c} \times 1000 \quad (1)$$

$$\eta_{POLE} = \frac{W_c}{W_A} \quad (2)$$

Where T_{OL} is oxide layer thickness (μm), W_c is oxide layer weight (mg), which is equal to the difference between the specimen weight after anodizing (W_2) and specimen weight after stripping (W_3), S is the oxide layer area in square millimeters (mm^2), and d_c is the oxide layer density (g/cm^3). The oxide layer density is $2.6 \text{ g}/\text{cm}^3$ for sealed oxide layer). η_p is the practical oxide layer efficiency, W_A is the weight of metal removed in milligrams (mg), which is equal to the difference between the specimen weight before anodizing (W_1) and specimen weight after stripping (W_3). The practical oxide layer efficiency represents the weight of the anodic layer that is formed on the metal surface divided by the weight of the total aluminum oxide formed. In other words, it is a coating ratio that reflects the amount of actual layer that acts as coating.

2.3. Electrochemical measurements

Electrochemical tests were carried out using a typical three-electrode

cell. The setup consisted of a calomel reference electrode (CRE), a platinum counter electrode (PCE), and a 1 cm² aluminum working electrode immersed in 0.5 M NaCl solution. The open-circuit potential (OCP) was measured after 150 minutes. Polarization measurements were performed under various conditions, both with and without the anodic film, at a scan rate of 1 mV per second within a range of -100 to +100 mV around the OCP. Electrochemical impedance spectroscopy (EIS) was carried out with a signal amplitude of 10.0 millivolts over a

second-order model has been used to fit the data, as shown in Eq. 4. Eq. 4 has been expanded in term of four variables as shown in Eq. 4a for the real variables and Eq. 4b for the coded variables.

$$Y = h_0 + \sum_{i=1}^k h_i X_i + \sum_{i=1}^k h_{ii} X_i^2 + \sum_{i=1}^{k-1} \sum_{j=i+1}^k h_{ij} X_i X_j + e \tag{4}$$

$$T_{OL} = h_0 + h_1 V_1 + h_2 V_2 + h_3 V_3 + h_4 V_4 + h_{11} V_1^2 + h_{22} V_2^2 + h_{33} V_3^2 + h_{44} V_4^2 + h_{12} V_1 V_2 + h_{13} V_1 V_3 + h_{14} V_1 V_4 + h_{23} V_2 V_3 + h_{24} V_2 V_4 + h_{34} V_3 V_4 + e \tag{4a}$$

$$Y_{OL} = h_0 + h_1 X_1 + h_2 X_2 + h_3 X_3 + h_4 X_4 + h_{11} X_1^2 + h_{22} X_2^2 + h_{33} X_3^2 + h_{44} X_4^2 + h_{12} X_1 X_2 + h_{13} X_1 X_3 + h_{14} X_1 X_4 + h_{23} X_2 X_3 + h_{24} X_2 X_4 + h_{34} X_3 X_4 + e \tag{4b}$$

frequency range from 10 kilohertz to 0.01 kilohertz. All electrochemical analyses were conducted using the Vertex-One potentiostat from the Netherlands.

2.4. Doehlert experimental design

The Doehlert experimental design was employed to construct the test set and optimize the anodizing process. Four variables (V_j) were used during the study. V_1 , V_2 , V_3 , and V_4 represent temperature (°C), electrolyte concentration (g/l), current density (A/dm²), and exposure time (min), respectively. The response function was assessed at various levels of the variables. The mixed OPA electrolytes concentration levels were 7 (5, 10, 15, 20, 25, 30, 35 g/L), temperature levels were 5 (25, 30, 35, 40, and 45 °C), current density levels were 7 (0.5, 1, 1.5, 2, 2.5, 3 and 3.5 A/dm²), and exposure time levels were 3 (10, 30, and 50 min.). The real variables were converted to the coded one using Eq. 3.

$$X_j = \frac{V - V(0)}{\Delta V_j} \tag{3}$$

Here X_j in code format, $V_j(0)$ in center and ΔV_j is step of variation. A

Table 1

Matrix of Doehlert experimental design for real and coded variables and oxidizing process outcomes (film thickness and practical oxide layer efficiency) at different conditions.

Exp. no.	X_1	X_2	X_3	X_4	V_1 (°C)	V_2 (g/l)	V_3 (A/dm ²)	V_4 (min)	T_{OL} (µm)	η_{POLE}
Code variables				Real variables						
1	1	0	0	0	45	20	2	30	17.4	0.76
2	0.5	0.866	0	0	40	35	2	30	14.7	0.65
3	-0.5	0.866	0	0	30	35	2	30	12.9	0.61
4	-1	0	0	0	25	20	2	30	21.1	0.93
5	-0.5	-0.866	0	0	30	5	2	30	18.2	0.88
6	0.5	-0.866	0	0	40	5	2	30	18.3	0.87
7	0.5	0.289	0.816	0	40	25	3.5	30	9.9	0.55
8	-0.5	0.289	0.816	0	30	25	3.5	30	16.2	0.75
9	0	-0.577	0.816	0	35	10	3.5	30	16.8	0.79
10	0.5	-0.289	-0.816	0	40	15	0.5	30	15.6	0.69
11	-0.5	-0.289	-0.816	0	30	15	0.5	30	16.5	0.78
12	0	0.577	-0.816	0	35	30	0.5	30	16.8	0.80
13	0.5	0.289	0.204	0.791	40	25	2.5	50	25.5	0.95
14	-0.5	0.289	0.204	0.791	30	25	2.5	50	15.9	0.69
15	0	-0.577	0.204	0.791	35	10	2.5	50	17.7	0.78
16	0	0	-0.612	0.791	35	20	1	50	15.6	0.71
17	0.5	-0.289	-0.204	-0.791	40	15	1.5	10	22.2	0.94
18	-0.5	-0.289	-0.204	-0.791	30	15	1.5	10	8.4	0.51
19	0	0.577	-0.204	-0.791	35	30	1.5	10	8.1	0.48
20	0	0	0.612	-0.791	35	20	3	10	7.8	0.43
21	0	0	0	0	35	20	2	30	26.5	0.96
22	0	0	0	0	35	20	2	30	25.5	0.95
23	0	0	0	0	35	20	2	30	24.4	0.94
24	0	0	0	0	35	20	2	30	24.7	0.94
25	0	0	0	0	35	20	2	30	23.9	0.93

$$\frac{\partial T_{OL}}{\partial V_3} = h_3 + 2h_{33}V_3 + h_{31}V_1 + h_{32}V_2 + h_{34}V_4 = 0$$

$$\frac{\partial T_{OL}}{\partial V_4} = h_4 + 2h_{44}V_4 + h_{41}V_1 + h_{42}V_2 + h_{43}V_3 = 0$$

Rearrange in term of matrix notation and Applying Cramer's rule, Eq. 6 can be solved for optimum conditions.

$$\begin{bmatrix} 2h_{11} & h_{12} & h_{13} & h_{14} \\ h_{21} & 2h_{22} & h_{23} & h_{24} \\ h_{31} & h_{32} & 2h_{33} & h_{34} \\ h_{41} & h_{42} & h_{43} & 2h_{44} \end{bmatrix} \begin{bmatrix} V_1 \\ V_2 \\ V_3 \\ V_4 \end{bmatrix} = \begin{bmatrix} -h_1 \\ -h_2 \\ -h_3 \\ -h_4 \end{bmatrix} \quad (6)$$

2.5. Surface morphological methods

$$T_{OL} = -95.28 + 4.62 V_1 + 0.78 V_2 + 17.01 V_3 + 0.79 V_4 - 0.06 V_1^2 - 0.03 V_2^2 - 3.14 V_3^2 - 0.02 V_4^2 + 0.01 V_1V_2 - 0.19V_1V_3 - 0.01V_1V_4 - 0.15 V_2V_3 + 0.02 V_2V_4 + 0.16 V_3V_4 \quad (4c)$$

$$Y_{OL} = 25.06 + 1.07 X_1 - 2.37 X_2 - 1.11X_3 + 4.46X_4 - 5.81X_1^2 - 10.11X_2^2 - 10.67X_3^2 - 10.53X_4^2 + 0.98X_1X_2 - 3.66X_1X_3 - 2.07 X_1X_4 - 4.69 X_2X_3 + 7.09 X_2X_4 + 5.73 X_3X_4 \quad (4d)$$

Surface morphological studies were achieved using the scanning electron microscope (SEM) to examine the surface morphology of the 4643 Al alloy surface in the absence and presence of oxide layer at optimum conditions. Quanta 200 scanning electron microscope (Dutch) was used for SEM images.

3. Results and discussion

3.1. The model regression and optimization

The outcomes of the anodizing process are collected in Table 1, which shows the oxide layer thickness and practical oxide layer efficiency. These two responses were fitted to a second-order polynomial. This regression process is widely used in scientific applications [29,30]. The non-linear (quadratic) mathematical polynomial models were

Table 2

Optimum conditions of variables for maximum oxide layer thickness and practical oxide layer efficiency.

Variable	Oxide layer thickness		Practical oxide layer efficiency	
	Real	Code	Real	Code
X ₁ , Temperature (°C)	35.565	0.054	34.071	- 0.092
X ₂ , Electrolytes concentration (g/L)	19.176	- 0.048	16.482	- 0.219
X ₃ , Current density (A/dm ²)	2.030	0.001	2.164	0.074
X ₄ , Exposure time (min.)	34.811	0.190	34.511	0.163
Optimum	25.5459 μm		0.976	

processed using the Levenberg-Marquardt least-squares method. Two equations were obtained (Eqs. 4c and 4d) with a high value of the correlation coefficient (R² greater than 0.9).

Similar regression analysis has been achieved for practical oxide layer efficiency (η_{POLE}).

$$\eta_{POLE} = -1.54 + 0.09V_1 + 0.02 V_2 + 0.38 V_3 + 0.03 V_4 - 0.001 V_1^2 - 0.001 V_2^2 - 0.07 V_3^2 - 0.001V_4^2 + 0.001 V_1V_2 - 0.004 V_1V_3 - 0.003 V_1V_4 - 0.006 V_2V_3 + 0.001 V_2V_4 + 0.005 V_3V_4 \quad (4e)$$

$$Y_{POLE} = 0.95 + 0.01 X_1 - 0.12 X_2 - 0.04X_3 + 0.121X_4 - 0.11X_1^2 - 0.226 X_2^2 - 0.25X_3^2 - 0.3 X_4^2 + 0.03 X_1X_2 - 0.08X_1X_3 - 0.097 X_1X_4 - 0.19 X_2X_3 + 0.21 X_2X_4 + 0.19 X_3X_4 \quad (4f)$$

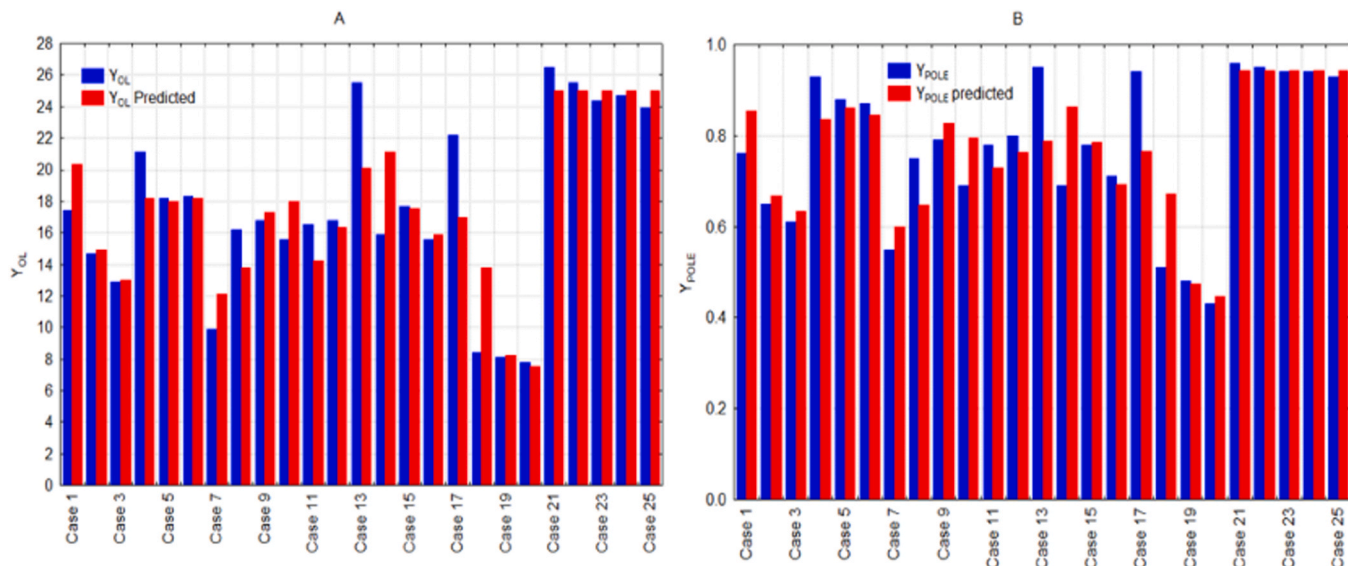


Fig. 1. The predicted and measured outcomes for the 25 experiments (A) oxide layer thickness and (B) practical oxide layer efficiency.

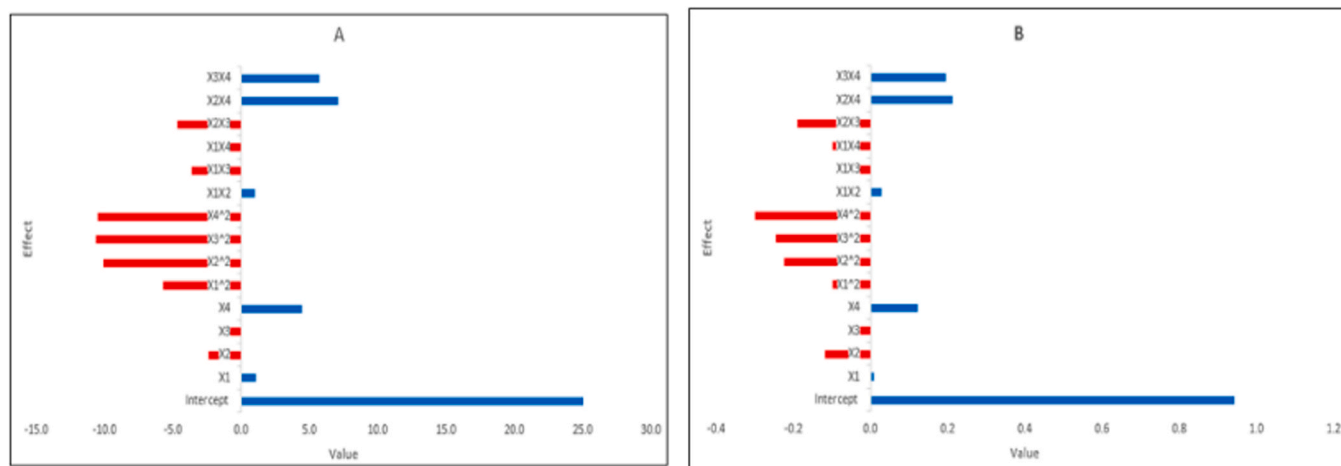


Fig. 2. Pareto chart for coded variable (A) oxide layer thickness and (B) practical oxide layer efficiency.

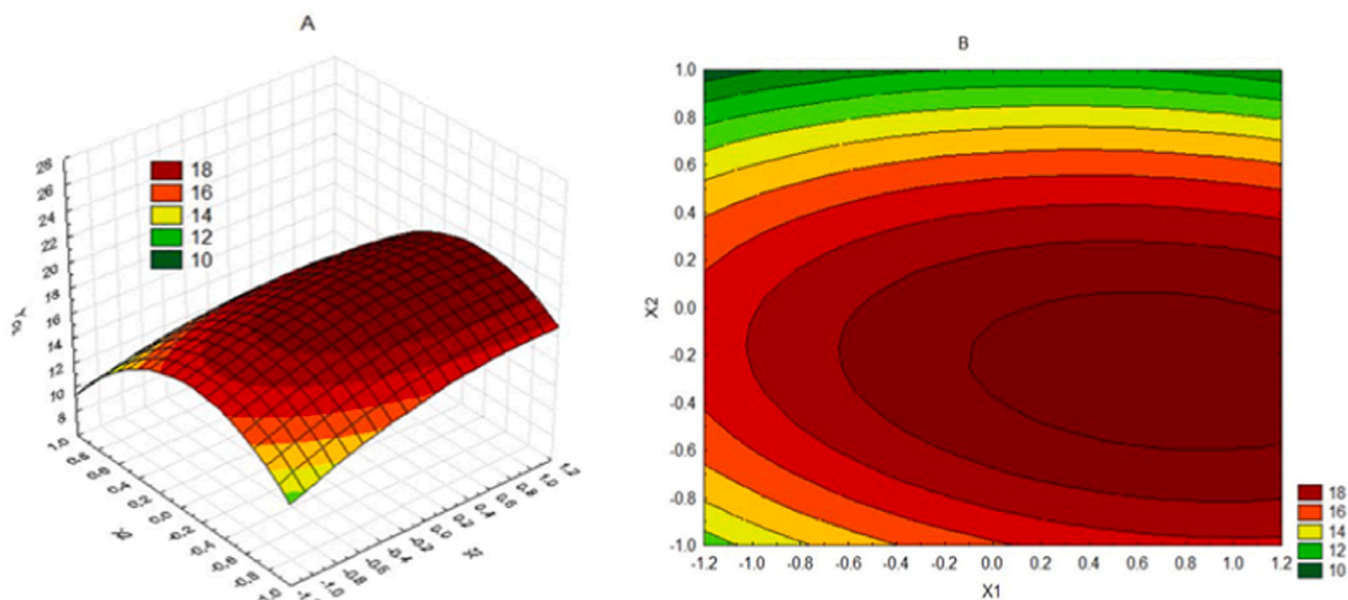


Fig. 3. Response surface plots (A) and contour plot (B) showing the variation of Y_{OL} as a function of anodizing process variables ($X_1 - X_4$).

Fig. 1a and b show the predicted results against experimental oxide layer thickness and practical oxide layer efficiency, respectively. This indicates a significant approach between the predicted and experimental values. Moreover, Eqs. 4c and 4d can be optimized to determine the optimal conditions. Table 2 shows the optimum process variables. The predicted oxide layer thickness and practical oxide layer efficiency were equal to 25.5459 μm and 0.976 under optimal conditions of V_1 , V_2 , V_3 , and V_4 , respectively. The enhanced thickness of the higher oxide layer was indicated by the increased formation rate of the anodic coating layer, which exceeded the rise in the dissolving rate of the anodic coating. Thus, the positive net effect resulting from these two factors is reflected in the augmentation of the film thickness. In Eq. 4d, the linear coefficients for the process variables (X_1 , X_2 , X_3 , and X_4) were 1.07, -2.373 , -1.102 , and 4.4571, respectively. The constants or coefficients of the model show that the effect of each factor on the rate of anodic coating layer formation can be ordered as $X_4 > X_2 > X_3 > X_1$, and the rate of dissolution is affected by increasing electrolyte temperature, mixed OPA electrolyte concentration, current density, and exposure time. The experimental oxide layer thickness closely matched the predicted value, demonstrating good agreement between them.

Additionally, the average absolute error percentage ($|e_i|$) was relatively low.

Fig. 2a and b (Pareto chart) show that the individual and interaction effects of the process factors upon the anticipated oxide layer thickness and practical oxide layer efficiency, respectively. A Pareto chart illustrates sequential relevance by displaying absolute values from the highest standardized effect to the smallest one. The figure also shows a reference line that is crossed by statistically significant parameters [31]. It is evident that both temperature and time positively influence oxide layer thickness and practical oxide layer efficiency, whereas electrolyte concentration and current density have a negative impact. The interaction effect among process variables varies from a negative to a positive effect on the anodizing process.

The optimum condition and active process zones are illustrated. Fig. 3A shows the surface plot of Y_{OL} as a function of X_1 and X_2 , while Fig. 3B shows the contour plot of Y_{OL} as a function of X_1 and X_2 . Similar figures at other conditions were given in the supplementary file (1S). On the other hand, Fig. 4A shows the surface plot of Y_{POLE} as a function of X_1 and X_2 , while Fig. 4B shows the contour plot of Y_{POLE} as a function of X_1 and X_2 . Similar figures at other conditions were given in the

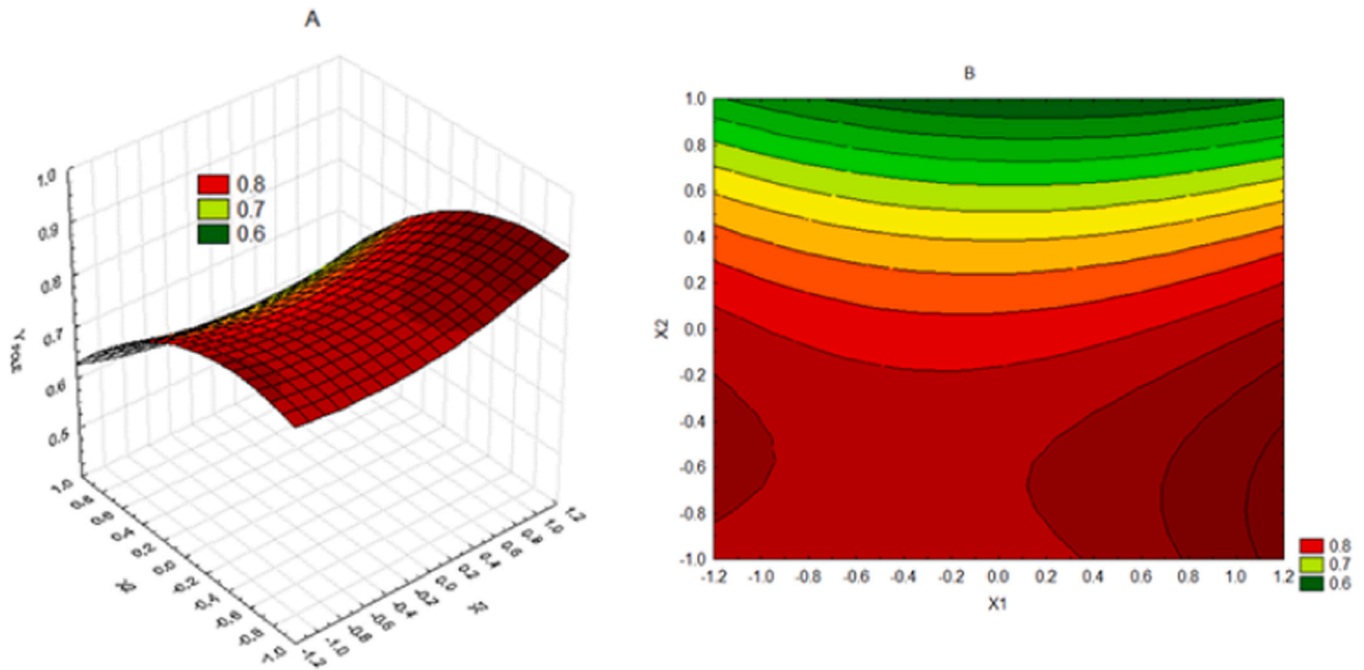


Fig. 4. Response surface plots (A) and contour plot (B) showing the variation of Y_{POLE} as a function of anodizing process variables ($X_1 - X_4$).

supplementary file (2S). The orange to dark red color zone represents the high level of response function, while the yellow to green color zone represents the low level.

3.2. Electrochemical studies

The electrochemical behavior of the anodized aluminum was assessed in a corrosive solution containing 0.5 M NaCl at 30°C. Three electrochemical measurements were conducted: open circuit potential (OCP), potential dynamic polarization (PDP), and electrochemical impedance spectroscopy (EIS). Ten samples at different anodization thicknesses were tested during the electrochemical measurements. In OCP measurements, Fig. 5 A shows the variation of potential with time for different thicknesses of anodized and bare aluminum in the aggressive 0.5 M NaCl solution. The steady-state potential was approached after 40 minutes. The OCP value of the bare Al was -0.748 V, as shown in Table 3. In the case of anodized aluminum, the observed OCP values shifted in a positive direction. This can be attributed to the presence of an aluminum oxide layer on the metal surface. In PDP measurements, Fig. 5B shows the variation of potential with current density. In addition, Table 3 collects the electrochemical parameters, including corrosion potential (E_{corr}), corrosion current density (i_{corr}), Tafel slopes (β_a and β_c), resistance polarization (R_p), and coating inhibition efficiency ($\%IE_{PDP}$). The values of R_p and $\%IE_{PDP}$ were calculated using Eq. 5 [32] and 6 [33], respectively.

$$R_p = \frac{\beta_a \beta_c}{2.303 i_{corr} (\beta_a + \beta_c)} \quad (5)$$

$$\%IE_{PDP} = \left(\frac{i_{corr} - i_{corr}^o}{i_{corr}} \right) \times 100 \quad (6)$$

In Eq. 6, i_{corr} and i_{corr}^o denote the corrosion current densities in the absence and presence of the coating layer, respectively. As shown in Table 3, the values of corrosion potentials were shifted in the positive direction in the presence of anodized layers. Additionally, corrosion current densities were observed to decrease in the case of anodized aluminum compared to the bare metal. It is clear that the maximum coating inhibition efficiency was 97 % at a 25.5 μm oxide coating layer. The values of Tafel slopes were approximately unchanged with the

presence of the oxide layer, which may mean unchanged in the kinetics and mechanism of the aluminum corrosion process. Electrochemical impedance spectroscopy (EIS) is an important analytical method to study the characteristics of the metal surface layer. It is a potent method for evaluating the corrosion resistance and structure of anodic oxide layers on the aluminum surface [34]. The data is fitted to the equivalent circuit. Fig. 5 C shows the Nyquist plots and equivalent circuit of the anodic oxide at different thicknesses immersed in a 0.5 M NaCl solution. The impedance of all the samples showed only one time constant, a capacitive loop, in the Nyquist plot. The semicircle's diameter grows as layer thickness increases. The resistance efficiency of the corrosive solution can be obtained using Eq. 7, using the resistance polarization values in the presence (R_p^o) and absence (R_p) of the oxide layer [35].

$$\%IE_{EIS} = \left(\frac{R_p^o - R_p}{R_p^o} \right) \times 100 \quad (7)$$

Table 4 collects the EIS parameters, which include the solution resistance (R_s), resistance polarization (R_p), capacitance of the double layer (C_{dl}), and $\%IE_{EIS}$ at different oxide layer thicknesses.

(1) 25.5 μm T_{OL} & 0.98 η_{Pole} (2) 22.2 μm T_{OL} & 0.94 η_{Pole} (3) 18.3 μm T_{OL} & 0.87 η_{Pole} (4) 17.7 μm T_{OL} & 0.78 η_{Pole} (5) 16.8 μm T_{OL} & 0.80 η_{Pole} (6) 14.7 μm T_{OL} & 0.65 η_{Pole} (7) 12.9 μm T_{OL} & 0.61 η_{Pole} (8) 9.9 μm T_{OL} & 0.55 η_{Pole} (9) 8.4 μm T_{OL} & 0.51 η_{Pole} (10) 7.8 μm T_{OL} & 0.43 η_{Pole} .

3.3. Morphology of the surface

Scanning electron microscopy (SEM) was used to analyze the surface morphology of aluminum under ideal conditions. The images are presented in Fig. 6. In Fig. 6A, the polished aluminum surface displays a smooth texture. Fig. 6B showcases the anodized aluminum surface, revealing pores that are uniformly distributed and arranged in a hexagonal honeycomb structure. This observation aligns with similar findings reported by Sun et al. [6] and Bensalah et al. [22]. In Fig. 6C, a cross-sectional view of the aluminum surface with the oxide layer thickness (T_{OL}) at optimum conditions is depicted, indicating the formation of an oxide-aluminum layer. Cross-sectional SEM image allowed for the diagnosis of the anodized coating thickness. Fig. 6D and E illustrate the top and cross-sectional views, respectively, of the stripped

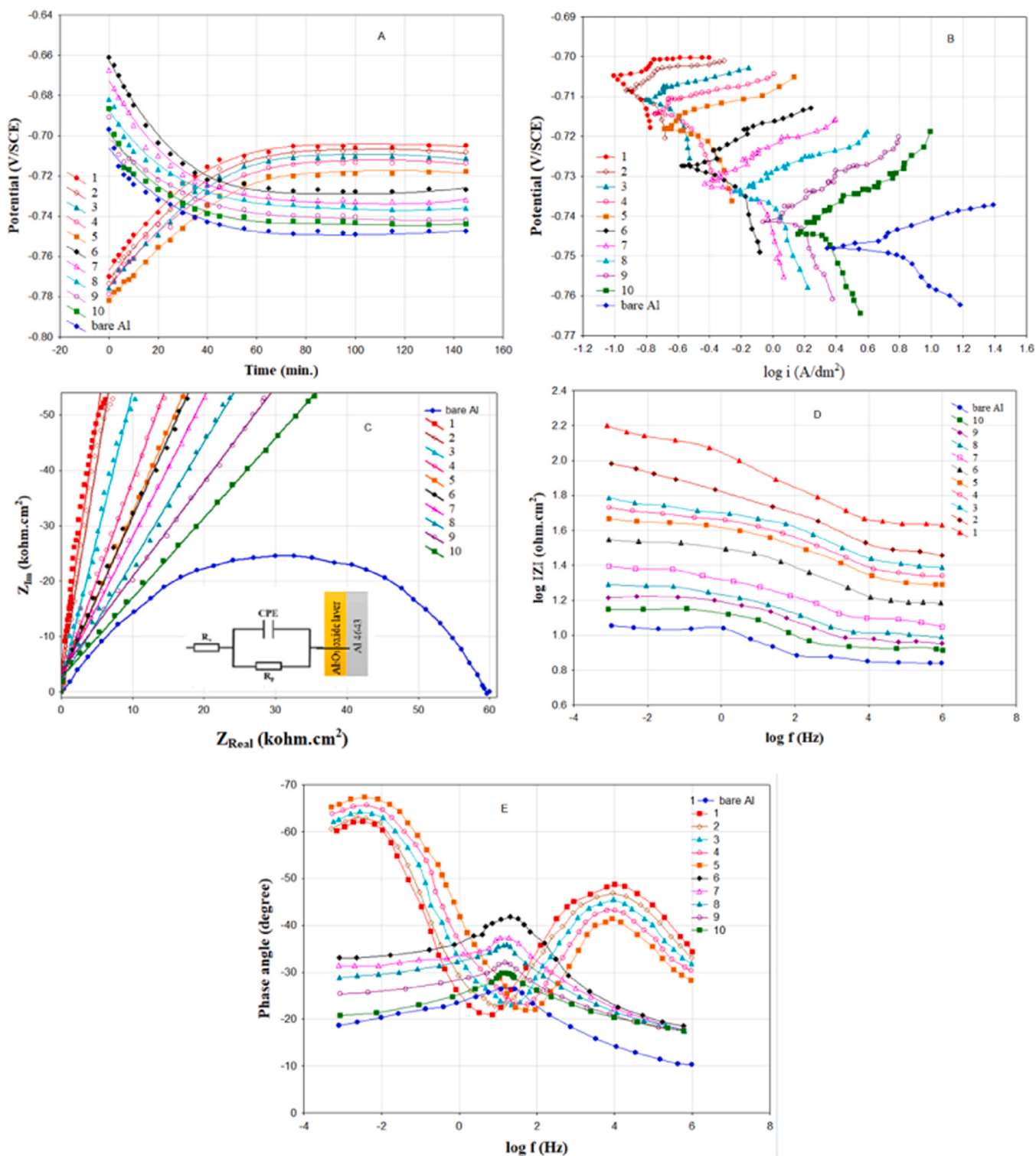


Fig. 5. (A) Open corrosion potential and (B) polarization curves (C) Nyquist (D) bode impedance (E) bode phase angle plots for the anodized Al 4643 aluminum alloy at the optimum conditions immersed in 0.5 M NaCl at 30 °C.

surface. The absence of the protective layer showed the damages of the metal surface.

3.4. Mechanism of anodizing process

Anodizing is an electrochemical technique that includes oxidizing a metal surface, usually aluminum, to form a porous and durable coating. Anodic aluminum oxide films are often classified into two types: porous

oxide films and nonporous barrier oxide films. The anodizing electrolyte used determines how these two types of films form. In neutral electrolytes, a solid, nonporous barrier-type layer that is nearly insoluble can emerge [36]. On the other hand, in acidic electrolytes, a porous-type layer can form momentarily, as the anodic oxide formed is minimally soluble [37,38]. The formation of anodic alumina occurs rapidly at the interfaces of the oxide/electrolyte and metal/oxide for the barrier-type oxide, facilitated by the outward flow and inward migration of

Table 3

Electrochemical parameters of 4643 Al alloy anodized in mixed OPA electrolytes at optimum & different other conditions.

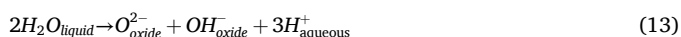
Specimen symbol	T _{OL} (μm)	OCV (V/SCE)	i _{corr} (A/dm ²)	E _{corr} (V/SCE)	β _a (mV/dec)	β _c (mV/dec)	R _p (Ω.cm ²)	η _{Pole}	IE _{PDP} (%)
1	25.5	-0.705	0.1122	-0.7051	180	-202	36.80	0.98	0.97
2	22.2	-0.708	0.1445	-0.7086	165	-201	27.20	0.94	0.96
3	18.3	-0.712	0.2138	-0.7109	145	-172	16.08	0.87	0.94
4	17.7	-0.714	0.2570	-0.7144	176	-202	15.92	0.78	0.92
5	16.8	-0.718	0.3162	-0.7182	171	-200	12.68	0.80	0.90
6	14.7	-0.727	0.4266	-0.7275	167	-207	9.41	0.65	0.87
7	12.9	-0.732	0.5888	-0.7318	147	-219	6.50	0.61	0.82
8	9.9	-0.736	0.9072	-0.7357	151	-221	4.30	0.55	0.73
9	8.4	-0.742	1.4894	-0.7414	160	-226	2.74	0.51	0.56
10	7.8	-0.744	2.0188	-0.7446	161	-230	2.04	0.43	0.42
Bare	-	-0.748	3.4565	-0.7482	162	-235	1.21	-	-

Table 4

The parameters values of equivalent circuit used for fitting the impedance measurements corresponding to the unprotected & the different protected surfaces thickness for Al 4643 alloy specimen's conditions.

Specimen symbol	T _{OL} (μm)	Rs (kΩ.cm ²)	R _p × 10 ⁻⁵ (kΩ.cm ²)	C _{dl} (μF.cm ⁻²)	% IE _{EIS}
bare	-	0.693	0.687	5.452	-
1	25.5	0.425	9.911	1.991	93.0
2	22.2	0.285	9.412	1.874	92.7
3	18.3	0.244	8.753	1.789	92.1
4	17.7	0.217	8.151	1.761	91.5
5	16.8	0.195	7.652	1.674	91.0
6	14.7	0.153	7.514	1.583	90.8
7	12.9	0.112	6.781	1.531	89.8
8	9.9	0.972	2.112	1.492	67.3
9	8.4	0.891	1.556	1.415	55.7
10	7.8	0.818	1.198	1.381	42.4

Al³⁺ and O²⁻/OH⁻ ions. However, for the porous-type oxide, oxide formation occurs primarily at the metal/oxide interface due to the inward migration of O²⁻/OH⁻ ions. Studies have observed that outward migrating Al³⁺ cations do not contribute to oxide growth at the oxide/electrolyte interface but are instead entirely released into the anodizing electrolyte through direct ejection [39,40]. Otherwise, outwardly migrating Al³⁺ ions would induce the formation of anodic alumina at the oxide/electrolyte interface, potentially sealing any pores that may have formed. The suggested elementary chemical processes occur at the metal/oxide interface (Eqs. 8 and 9) and the oxide/electrolyte contact (Eqs. 10–13):



In both nonporous and porous oxide films, Eq. 9 describes the formation of anodic oxide at the metal/oxide and oxide/electrolyte interfaces. Eq. 10 accounts for the dissolution of anodic alumina. Eq. 11 occurs due to the field-assisted direct ejection of Al³⁺ ions from the metal/oxide interface into the electrolyte through the oxide. Eqs. 11–13 collectively reduce the net current efficiency associated with anodic oxide generation. At the oxide/electrolyte interface, water molecules undergo heterolytic breakdown, leading to the formation of oxygen anions at the metal/oxide contact and consequent creation of anodic oxide, as detailed in Eq. 13. It is assumed that all oxide anions resulting

from the dissolution of Al₂O₃ at the oxide/electrolyte interface migrate to the metal/oxide interface, where they are utilized to reconstruct Al₂O₃. Additionally, the production of oxide is influenced by all oxide anions generated from water dissociation [40]. The anodizing process can potentially be enhanced by the presence of organic acids, which supply reactive species. Analyzing the chemical composition of the protective layer may require extensive investigation under both electrolyte-absent and electrolyte-present conditions. However, a schematic representation of both oxide films and the proposed anodizing process for porous anodic films can be found in Fig. 7. However, the corrosion resistance of porous anodic alumina films at different locations is not uniform on the metal surface. This can be attributed to the different degrees of anion adsorption. In other words, the growing porous anodic alumina film is concurrently subjected to the electrolyte corrosion [41]. This is highly dependent on several factors. An increase in electrolyte temperature would aggravate the selective corrosion during the growth of porous anodic alumina film. On the other hand, an increase in electrolyte concentration would influence the anodizing voltage. This will reduce the pore distance of the porous anodic alumina film [42].

3.5. Comparative study and the role of optimization process

The oxide layer thickness that formed during the anodizing process depends on many factors, and it varies from one metal alloy to others. According to Elkilany et al. [41], who studied the anodizing process of aluminum alloys 2014-T3, 6061-T6, and 7075-T6 in sulfuric acid, 7075-T6 aluminum alloy has the highest thickness. While the presence of Fe and Si in 6061 Al alloy delays the oxide growth. The lowest thickness of the oxide layer was formed on the 2014 Al alloy, which can be attributed to the high content of copper. During 60 minutes in 17 % H₂SO₄ electrolyte and 2.8 A/dm², the coating thickness varies approximately from 5 to 50 μm for all aluminum alloys. Chung et al. [42] investigated the anodizing of 6061 aluminum alloy in an H₂SO₄ electrolyte. They found that increasing the current density enhanced the thickness of the oxidized films. The film thickness ranged from 1.46 to 25.75 μm, which agreed with current work. Bononi et al. [42] studied the anodizing of AA2099-T8 in sulfuric solution as a function of temperature, cation concentration, and current. The hardness of the oxide layer increased with temperature decreases. At all tested conditions, the oxide layer thickness was around 55 ± 5 μm. Lu et al. [17] obtained an optimum film thickness of 50 μm on the AA2024 aluminum surface, which was anodized in a mixed acid system of sulfuric and malonic acid. Kikuchi et al. [14] found anodic porous alumina thicknesses in etidronic acid. The film thicknesses were 42 mm and 77 mm at 270 V and 293 K for 2 h and 270 V and 273 K for 72 h, respectively. These results showed higher film thickness as compared with the results of the present study, which can be attributed to high exposure time. However, the optimization process represented a powerful tool in the estimation of the optimum anodization conditions. On the other hand, the obtained mathematical model can be used successfully in predicting the formed

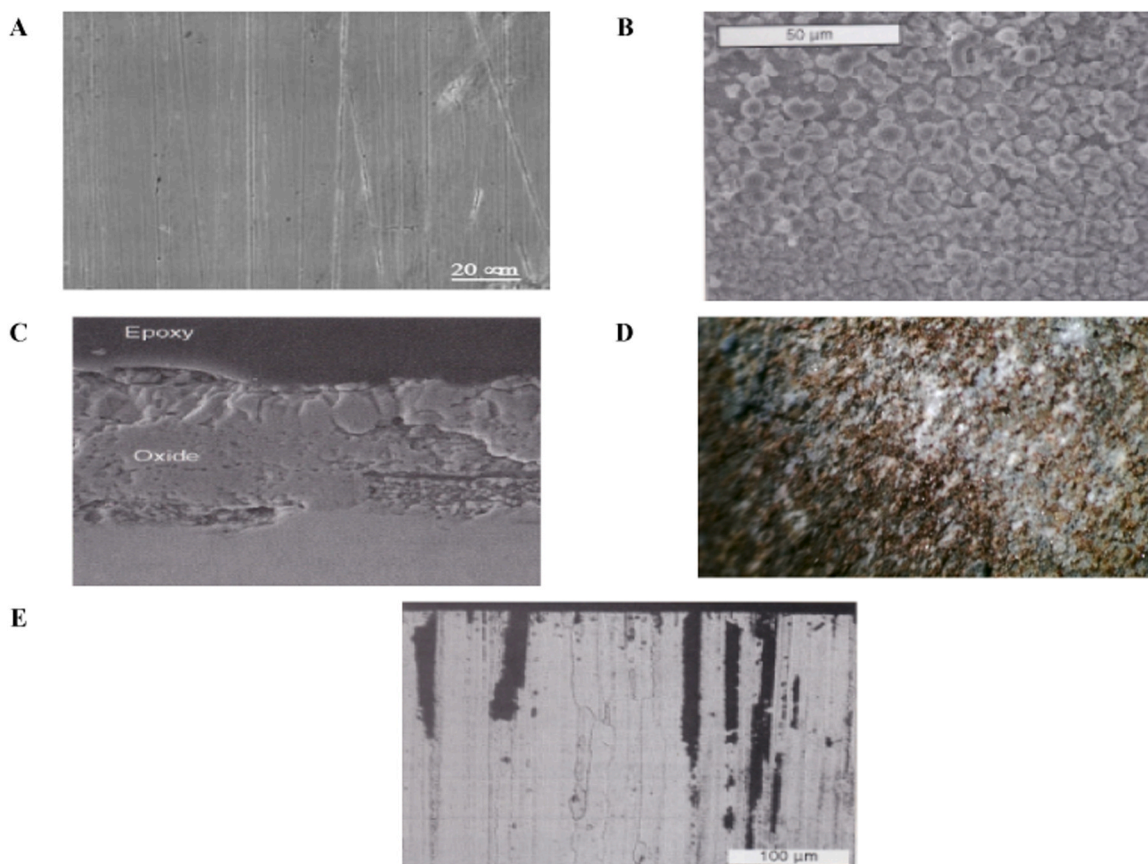


Fig. 6. Surface electron microstructure of Al 4643 aluminum alloy (A) polished Al surface, (B) top view appearance of surface T_{OL} at optimum conditions & 34.8 min. (C) cross section views of surface T_{OL} at optimum conditions & 34.8 min., (D) top view of stripped surface T_{OL} , (E) cross section views of stripped surface T_{OL} .

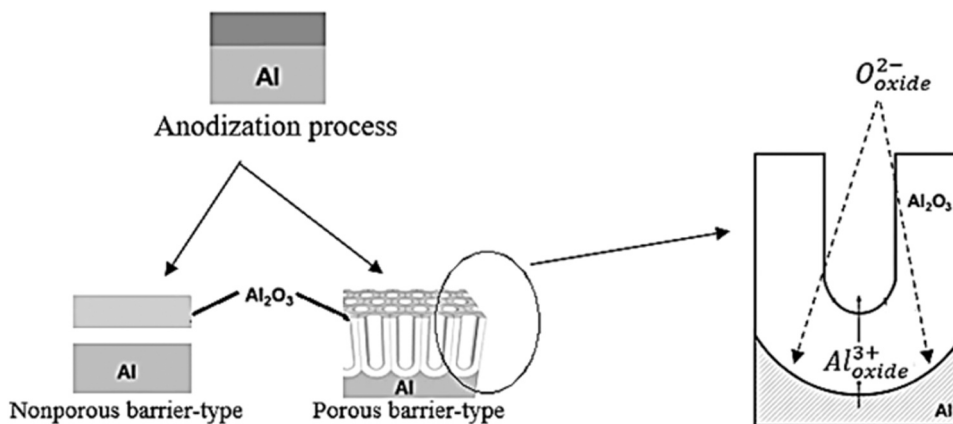


Fig. 7. Nonporous and porous barrier films and the proposed mechanism for the porous one.

film thickness and wide operating conditions. Moreover, the approach between oxide layer thickness for different types of aluminum alloys may assist in the use of a mathematical model for other aluminum alloys.

3.6. Drawback and limitations of anodizing process

Although the anodization of aluminum provides excellent corrosion resistance and durability, it also has some drawbacks. These included mechanical, chemical, appealing, economic, and environmental drawbacks [43,44]. In mechanical drawbacks, the strength of metal may be reduced due to the removal of the surface material. Furthermore, the

anodization process may increase the surface roughness. Chemical drawbacks affected the metal surface due to the penetration of chemicals through the porous structure, which leads to corrosion problems. Color inconsistency and discoloration can be the main problems of appealing drawbacks. Relatively, the anodization technology adds processing and production time. In addition, it generates waste that requires a suitable disposal procedure. Ecological problems can be due to the volatilization of organic electrolyte solutions, which in turn leads to air pollution. Furthermore, chemical effluent produces wastewater containing acids, heavy metals, and other pollutants, which lead to water pollution. Economical issues are adding other drawbacks due to the energy and

water consumption.

4. Conclusion

The Doehlert experimental design proven to be a durable instrument for exploring the behavior of anodic porous alumina film produced on an aluminum surface by anodizing in an oxalic/phosphoric electrolyte. The oxide layer thickness (T_{OL}) and the practical oxide layer efficiency (η_{POLE}) were influenced by temperature, electrolyte concentration, current density, and exposure time. The experimental design's outcomes show that every process-independent variable is crucial to the anodizing process. Furthermore, there is a noteworthy interaction effect of independent variables on both the practical oxide layer efficiency and thickness. The optimum T_{OL} and η_{POLE} are 25.5459 μm and 0.976, respectively. According to electrochemical techniques, the steady-state potentials are typically approached around the forty-minute mark. The corrosion current density dropped as layer thickness increased. At the ideal layer thickness, protection efficacy reached a maximum of 97 %. Measurements conducted using electrochemical impedance spectroscopy revealed that the resistance of the metal increased with the thickness of the layer, corroborating the findings from polarization experiments. The surface morphology studies were used to confirm the formation of the protective layer on aluminum surface.

CRedit authorship contribution statement

Khalid H. Rashid: Methodology, Formal analysis, Data curation, Conceptualization. **Abdul Amir H. Kadhum:** Visualization, Supervision. **Anees Khadom:** Writing – review & editing, Writing – original draft, Validation, Supervision, Software.

Declaration of Competing Interest

We wish to confirm that there are no known conflicts of interest associated with this publication and there has been no significant financial support for this work that could have influenced its outcome.

We confirm that the manuscript has been read and approved by all named authors and that there are no other persons who satisfied the criteria for authorship but are not listed. We further confirm that the order of authors listed in the manuscript has been approved by all of us.

We confirm that we have given due consideration to the protection of intellectual property associated with this work and that there are no impediments to publication, including the timing of publication, with respect to intellectual property. In so doing we confirm that we have followed the regulations of our institutions concerning intellectual property.

We understand that the Corresponding Author is the sole contact for the Editorial process (including Editorial Manager and direct communications with the office). He is responsible for communicating with the other authors about progress, submissions of revisions and final approval of proofs. We confirm that we have provided a current, correct email address which is accessible by the Corresponding Author and which has been configured to accept email from aneedr@gmail.com

Appendix A. Supporting information

Supplementary data associated with this article can be found in the online version at [doi:10.1016/j.ijoes.2025.100945](https://doi.org/10.1016/j.ijoes.2025.100945).

References

- [1] H. Rashid, A.A. Khadom, S.H. Abbas, K.F. Al-azawi, H.B. Mahood, Optimization studies of expired mouthwash drugs on the corrosion of aluminum 7475 in 1M hydrochloric acid: Gravimetric, electrochemical, morphological and theoretical investigations, *Results Surf. Interfaces* 13 (2023) 100165, <https://doi.org/10.1016/j.rsurfi.2023.100165>.
- [2] N. Birbilis, R.G. Buchheit, Electrochemical characteristics of intermetallic phases in aluminum alloys: an experimental survey and discussion, *B140-B151*, *J. Electrochem. Soc.* 152 (2005), <https://doi.org/10.1149/1.1869984>.
- [3] M. Vakili-Azghandi, A. Fattah-alhosseini, M.K. Keshavarz, Optimizing the electrolyte chemistry parameters of PEO coating on 6061 Al alloy by corrosion rate measurement: Response surface methodology, *J. Int. Meas. Confed.* 124 (2018) 252–259, <https://doi.org/10.1016/j.measurement.2018.04.038>.
- [4] Y. Chai, J. Yan, C. Wang, L. Mei, Effect of electrical parameters on the growth and properties of 7075 Aluminum alloy film based on scanning micro-arc oxidation with mesh electrode, *J. Mater. Res. Technol.* 988–998 (2023) 25, <https://doi.org/10.1016/j.jmrt.2023.06.020>.
- [5] Q. Wang, H. Li, Study on anodic oxidation of 2099 aluminum lithium alloy and sealing treatment in environmental friendly solutions, *Int. J. Electrochem. Sci.* 18 (2023) 100186, <https://doi.org/10.1016/j.ijoes.2023.100186>.
- [6] M. Sun, H. Huang, M. Jiang, L. Cheng, L. Dong, Influence of oxalic additive on etidronic acid anodizing of aluminum alloy, *J. Electroanal. Chem.* 944 (2023) 117641, <https://doi.org/10.1016/j.jelechem.2023.117641>.
- [7] A. Musza, D. Ugi, Á. Vida, N.Q. Chinh, Study of Anodic Film's Surface and Hardness on A356 Aluminum Alloys, Using Scanning Electron Microscope and In-Situ Nanoindentation, *Coatings* 12 (2022) 1528, <https://doi.org/10.3390/coatings12101528>.
- [8] L. Dong, Y. Li, M. Huang, X. Hu, Z. Qu, Y. Lu, Effect of anodizing surface morphology on the adhesion performance of 6061 aluminum alloy, *Int. J. Adhes. Adhes.* 113 (2021) 103065, <https://doi.org/10.1016/j.ijadhadh.2021.103065>.
- [9] C. Cabral, C.G. Tiburcio, F.E. López, P.Z. Robledo, F.O. Coca, L.L. León, J.Á. C. Miramontes, Citric Acid as an Alternative to Sulfuric Acid for Hard Anodizing in Aluminum Alloys Used in the Aeronautical Industry, *ECS Trans.* 110 (2023) 225–236, <https://doi.org/10.1149/11001.0225ecst>.
- [10] D. Nakajima, T. Kikuchi, S. Natsui, R.O. Suzuki, Growth behavior of anodic oxide formed by aluminum anodizing in glutaric and its derivative acid electrolytes, *Appl. Surf. Sci.* 321 (2014) 364–370, [https://doi.org/10.1016/S1003-6326\(16\)64137-7](https://doi.org/10.1016/S1003-6326(16)64137-7).
- [11] V.F. Surganov, G.G. Gorokh, Anodic oxide cellular structure formation on aluminum films in tartaric acid electrolyte, *Mater. Lett.* 17 (1993) 121–124, [https://doi.org/10.1016/0167-577X\(93\)90069-A](https://doi.org/10.1016/0167-577X(93)90069-A).
- [12] A. Mozalev, I. Mozaleva, M. Sakairi, H. Takahashi, Anodic film growth on Al layers and Ta–Al metal bilayers in citric acid electrolytes, *Electrochim. Acta* 50 (2005) 5065–5075, <https://doi.org/10.1016/j.electacta.2005.02.092>.
- [13] T. Kikuchi, O. Nishinaga, D. Nakajima, J. Kawashima, S. Natsui, N. Sakaguchi, R. O. Suzuki, Ultra-High Density Single Nanometer-Scale Anodic Alumina Nanofibers Fabricated by Pyrophosphoric Acid Anodizing, *Sci. Rep.* 4 (2014) 7411, <https://doi.org/10.1038/srep07411>.
- [14] T. Kikuchi, O. Nishinaga, S. Natsui, R.O. Suzuki, Fabrication of self-ordered porous alumina via etidronic acid anodizing and structural color generation from submicrometer-scale dimple array, *Electrochim. Acta* 156 (2015) 235–243, <https://doi.org/10.1016/j.electacta.2014.12.171>.
- [15] M. Saediikhani, M. Javidi, A. Yazdani, Anodizing of 2024-T3 aluminum alloy in sulfuric-boric-phosphoric acids and its corrosion behavior, *Trans. Nonferrous Met. Soc. China* 23 (2013) 2551–2559, [https://doi.org/10.1016/S1003-6326\(13\)62767-3](https://doi.org/10.1016/S1003-6326(13)62767-3).
- [16] Y. Shang, L. Wang, D. Niu, Z. Liu, Y. Wang, C. Liu, Effects of additive for anodizing electrolyte on anodic film of high silicon aluminum alloy, *Int. J. Electrochem. Sci.* 11 (2016) 1549–1557, [https://doi.org/10.1016/s1452-3981\(23\)15940-2](https://doi.org/10.1016/s1452-3981(23)15940-2).
- [17] J. Lu, G. Wei, Y. Yu, C. Guo, L. Jiang, Aluminum alloy AA2024 anodized from the mixed acid system with enhanced mechanical properties, *Surf. Interfaces* 13 (2018) 46–50, <https://doi.org/10.1016/j.surfint.2018.08.003>.
- [18] V.R. Capelossi, M. Poelman, I. Recloux, R.P.B. Hernandez, H.G. De Melo, M. G. Olivier, Corrosion protection of clad 2024 aluminum alloy anodized in tartaric-sulfuric acid bath and protected with hybrid sol–gel coating, *Electrochim. Acta* 124 (2014) 69–79, <https://doi.org/10.1016/j.electacta.2013.09.004>.
- [19] M. Kebir, I. Benramdhan, N. Nasrallah, H. Tahraoui, N. Bait, H. Benaisa, A. Amrane, A. Surface response modeling of homogeneous photo Fenton Fe (III) and Fe (II) complex for sunlight degradation and mineralization of food dye, *Catal. Commun.* 183 (2023) 106780, <https://doi.org/10.1016/j.catcom.2023.106780>.
- [20] D. Mansour, E. Alblawi, A. Alsukaibi, J. Humaidi, H. Tahraoui, M. Shatat, A. Amrane, Modeling and Optimization of Electrochemical Advanced Oxidation of Clopidogrel Using the Doehlert Experimental Design Combined with an Improved Grey Wolf Algorithm, *Water* 16 (2024) 1964, <https://doi.org/10.3390/w16141964>.
- [21] S.H. Abbas, Y.M. Younis, K.H. Rashid, A.A. Khadom, Removal of methyl orange dye from simulated wastewater by electrocoagulation technique using Taguchi method: kinetics and optimization approaches, *React. Kinet. Mech. Catal.* 135 (2022) 2663–2679, <https://doi.org/10.1007/s11144-022-02269-9>.
- [22] W. Bensalah, K. Elleuch, M. Feki, M. Depetris-Wery, H. Ayedi, Optimization of tartaric/sulphuric acid anodizing process using Doehlert design, *Surf. Coat. Technol.* 207 (2012) 123–129, <https://doi.org/10.1016/j.surfcoat.2012.06.059>.
- [23] M. Bargui, K. Elleuch, M. Wery, H. Ayedi, Optimization of mechanical and tribological properties of anodized 5754 aluminium alloy, *Surf. Eng. Appl. Electrochem.* 53 (2017) 371–382, <https://doi.org/10.3103/S1068375517040020>.
- [24] W. Bensalah, K. Elleuch, M. Feki, M. Depetris-Wery, H.F. Ayedi, Optimization of tartaric/sulphuric acid anodizing process using Doehlert design, *Surf. Coat. Technol.* 207 (2012) 123–129, <https://doi.org/10.1016/j.surfcoat.2012.06.059>.
- [25] M. Bargui, K. Elleuch, M. Wery, H.F. Ayedi, Optimization of mechanical and tribological properties of anodized 5754 aluminium alloy, *Surf. Eng. Appl. Electrochem.* 53 (2017) 371–382, <https://doi.org/10.3103/S1068375517040020>.

- [26] W. Bensalah, K. Elleuch, M. Feki, M. Wery, M.P. Gigandet, H.F. Ayedi, Optimization of mechanical and chemical properties of sulphuric anodized aluminium using statistical experimental methods, *Mater. Chem. Phys.* 108 (2008) 296–305, <https://doi.org/10.1016/j.matchemphys.2007.09.043>.
- [27] K.H. Rashid, A.A. Khadom, Sulfosalicylic/oxalic acid anodizing process of 5854 aluminum-magnesium alloy: influence of sealing time and corrosion tendency, *Results Chem.* 4 (2022) 100289, <https://doi.org/10.1016/j.rechem.2022.100289>.
- [28] K.H. Rashid, A.A. Khadom, H.B. Mahood, Aluminum ASA 6061 anodizing process by chromic acid using Box–Wilson central composite design: optimization and corrosion tendency, *Met. Mater. Int.* 27 (2021) 4059–4073, <https://doi.org/10.1007/s12540-020-00762-1>.
- [29] S. Zhang, J. Yu, Z. Liu, Y. Li, Modelling and optimization of electrodeposited amorphous Fe-P alloys using central composite design and response surface method, *Int. J. Electrochem. Sci.* 19 (2024) 100644, <https://doi.org/10.1016/j.ijoes.2024.100644>.
- [30] T. Su, M. Wang, K. Wang, W. Gao, Y. Gao, P. Gao, C. Lu, Optimized electrochemical treatment of semi-coking wastewater for enhanced degradation of biological toxicity using a Ru-Ir-Ti anode and Co-Ti cathode, *Int. J. Electrochem. Sci.* 19 (2024) 100718, <https://doi.org/10.1016/j.ijoes.2024.100718>.
- [31] F. Asen, M. Dehestani, Influence of concrete mix proportions on lifetime flexural load-bearing capacity of RC beams under chloride corrosion of rebars, *Structures* 29 (2021) 2017–2027, <https://doi.org/10.1016/j.istruc.2021.01.009>.
- [32] W. Nguyen, J.F. Duncan, T.M. Devine, et al., Electrochemical polarization and impedance of reinforced concrete and hybrid fiber-reinforced concrete under cracked matrix conditions, *Electrochim. Acta* 271 (2018) 319–336, <https://doi.org/10.1016/j.electacta.2018.03.134>.
- [33] O. Sanni, S.A. Iwarere, M.O. Daramola, Evaluation of corrosion inhibition of essential oil-based inhibitors on aluminum alloys, *ACS Omega* 7 (45) (2022) 40740–40749, <https://doi.org/10.1021/acsomega.2c00540>.
- [34] J. Hitzig, K. Jüttner, W.J. Lorenz, W. Paatsch, AC-impedance measurements on corroded porous aluminum oxide films, *J. Electrochem. Soc.* 133 (1986) 887–892, <https://doi.org/10.1149/1.2108756>.
- [35] M. Ouakki, M. Rbaa, M. Galai, B. Lakhri, E.H. Rifi, M. Cherkaoui, Experimental and Quantum Chemical Investigation of Imidazole Derivatives as Corrosion Inhibitors on Mild Steel in 1.0 M Hydrochloric Acid, *J. Bio-Tribo-Corros.* 4 (2018) 35, <https://doi.org/10.1007/s40735-018-0151-2>.
- [36] G.E. Thompson, Porous anodic alumina: fabrication, characterization and applications, *Thin Solid Films* 297 (1997) 192–201, [https://doi.org/10.1016/S0040-6090\(96\)09440-0](https://doi.org/10.1016/S0040-6090(96)09440-0).
- [37] S. Ono, M. Saito, H. Asoh, Self-ordering of anodic porous alumina formed in organic acid electrolytes, *Electrochim. Acta* 51 (2005) 827–833, <https://doi.org/10.1016/j.electacta.2005.05.058>.
- [38] S.Z. Chu, K. Wada, S. Inoue, M. Isogai, Y. Katsuta, A. Yasumori, Large-scale fabrication of ordered nanoporous alumina films with arbitrary pore intervals by critical-potential anodization, *J. Electrochem. Soc.* 153 (2006) 384–391, <https://doi.org/10.1149/1.2218822>.
- [39] Z. Wu, C. Richter, L. Menon, A study of anodization process during pore formation in nanoporous alumina templates, *J. Electrochem. Soc.* 154 (2007) 8–12, <https://doi.org/10.1149/1.2382671>.
- [40] W. Lee, S.J. Park, Porous anodic aluminum oxide: anodization and templated synthesis of functional nanostructures, *Chem. Rev.* 114 (2014) 7487–7556, <https://doi.org/10.1021/cr500002z>.
- [41] H. Elkilany, M. Shoeib, O. Abdel-Salam, Influence of hard anodizing on the mechanical and corrosion properties of different aluminum alloys, *Metallogr., Microstruct., Anal.* 8 (2019) 861–870, <https://doi.org/10.1007/s13632-019-00594-5>.
- [42] I. Chung, C. Chung, Y. Su, Effects of anodization parameters on the corrosion resistance of 6061 Al alloy using the Taguchi method, *Microsyst. Technol.* 24 (2018) 351–359, <https://doi.org/10.1007/s00542-017-3385-x>.
- [43] V. Mymrin, D. Pedroso, C. Pedroso, K. Alekseev, M. Avanci, E. Winter Jr, E. R. Catai, Environmentally clean composites with hazardous aluminum anodizing sludge, concrete waste, and lime production waste, *J. Clean. Prod.* 174 (2018) 380–388, <https://doi.org/10.1016/j.jclepro.2017.10.299>.
- [44] M. Souza, L. Simão, O. Montedo, F. Pereira, A. de Oliveira, Aluminum anodizing waste and its uses: an overview of potential applications and market opportunities, *Waste Manag.* 84 (2019) 286–301, <https://doi.org/10.1016/j.wasman.2018.12.003>.